Direct measurement of slip velocities using three-dimensional total internal reflection velocimetry

By PETER HUANG, JEFFREY S. GUASTO
AND KENNETH S. BREUER

Division of Engineering, Brown University, Providence, RI 02915, USA

The existence and magnitude of slip velocities between deionized water and a smooth glass surface is studied experimentally. Sub-micron fluorescent particles are suspended in water and imaged using total internal reflection velocimetry (TIRV). For water flowing over a hydrophilic surface, the measurements are in agreement with previous experiments and indicate that slip, if present, is minimal at low shear rates, but increases slightly as the shear rate increases. Surface hydrophobicity is observed to induce a small slip velocity, with the slip length reaching a maximum of 96 nm at a shear rate of $1800\,s^{-1}$. Issues associated with the experimental technique and the interpretation of results are also discussed.

1. Introduction

The century-old assumption of the no-slip boundary condition between a liquid and a solid has been challenged by recent experimental results and molecular dynamic simulations and has been the subject of many recent investigations exploring flows over both wetting and non-wetting surfaces. Although there is considerable disagreement regarding the existence of slip over a hydrophilic surface, it is generally believed that surface hydrophobicity aids slip, while the exact mechanism is not yet understood (for a review of this topic, see Lauga, Brenner & Stone 2005). Experimental studies have reported a wide range of slip lengths, ranging from micrometres (Schnell 1956; Watanabe, Yanuar & Mizunuma 1998; Zhu & Granick 2001; Tretheway & Meinhart 2002), hundreds of nanometres (Pit, Hervet & Leger 2000; Lumma *et al.* 2003), to tens of nanometres or smaller (including no-slip) (Zhu & Granick 2002; Choi, Westin & Breuer 2003; Neto, Craig & Williams 2003; Joseph & Tabeling 2005; Cottin-Bizonne *et al.* 2005*b*). Molecular dynamics simulations, on the other hand, suggest small slip lengths, mostly less than 100 nm (Thompson & Troian 1997; Barrat & Bocquet 1999; Cieplak, Koplik & Banavar 2001; Galea & Attard 2004; Nagayama & Cheng 2004; Cottin-Bizonne *et al.* 2005*a*).

The experiments have been conducted under various direct and indirect measurement techniques with varying accuracy and uncertainty. In indirect measurements, slip velocity is inferred from other flow quantities, such as the relationship between flow rate and pressure drop (Choi *et al.* 2003) or the measurement of the forces required to move a pair of crossed cylindrical surfaces separated by a thin film of the test fluid (Zhu & Granick 2001, 2002; Neto *et al.* 2003; Cottin-Bizonne *et al.* 2005*b*). In contrast, alternative techniques such as micro-particle image velocimetry

(PIV) have resulted in direct measurements of near-surface fluid velocity using tracer particles (Tretheway & Meinhart 2002; Joseph & Tabeling 2005).

Although the direct measurements have a strong appeal, there are two major drawbacks inherent to conventional micro-PIV. The first is that the velocity is determined from the motion of a collection of particles in an interrogation area (IA) and, in order to obtain a reasonable estimate of the velocity, the IA must be several hundred nanometres in size (Tretheway & Meinhart 2002). Hence the determination of phenomena which might measure a few nanometres is very difficult. A second problem is that the measurement volume along the optical axis for flood-illuminated micro-PIV techniques is defined by the focal depth of the optical system, which is typically of the order of 0.5 to 1 μm (Tretheway & Meinhart 2002; Joseph & Tabeling 2005). Although Joseph & Tabeling (2005) reported a slip length measurement with 100 nm resolution, micro-PIV would still be insufficient to provide an affirmative conclusion if the true slip length were below 100 nm.

An approach that solves both of these problems is the use of total internal reflection velocimetry (TIRV) (Jin *et al.* 2004) which uses total internal reflection of an incident laser pulse to generate a highly localized illumination of the surface flow, and relies on tracking the motion of single tracer particles rather than the collective particle motion that is used in PIV. Total internal reflection fluorescence microscopy (TIRFM) has long been used by biologists to study near-surface dynamics (Thompson & Langerholm 1997; Burmeister *et al.* 1998; Toomre & Manstein 2001). Zettner & Yoda (2003) combined micro-PIV and TIRFM to study near-surface Couette flow while Pit *et al.* (2000) measured slip velocity of hexadecane over a sapphire substrate using TIRFM and fluorescence recovery after photobleaching. Jin *et al.* (2004) first reported on the TIRV technique in the context of slip velocities for near-wall microflows, but were unable to determine the size or character of any slip lengths conclusively, owing to difficulties in the determination of the location of tracer particles within the narrow evanescent illumination region.

The present paper reports on experiments in which the TIRV technique has been substantially improved to the point that quantitative statements can be made regarding the nature of slip velocities over hydrophilic and hydrophobic surfaces. By measuring the intensity of the fluorescence of tracer particles, and in conjunction with a statistical model for the optical and hydrodynamic behaviour of small particles near a surface, we were able to track their motion within a narrow region above the solid surface and to compare that motion to the motion predicted for different levels of boundary slip.

2. Theoretical considerations

2.1. *Total internal reflection microscopy*

The evanescent field and its application to fluorescence microscopy has been well documented in literature (e.g. Hosoda, Sakai & Takagi 1998; Axelrod 2001; Zettner & Yoda 2003; Jin *et al.* 2004; Kihm *et al.* 2004; Sadr, Li & Yoda 2005). In summary, an evanescent field can be created near a solid–liquid interface where total internal reflection occurs (figure 1). The field intensity, I, decays exponentially with distance, z, away from the two-medium interface by

$$I(z) = I_0 e^{-z/p}, \qquad (2.1)$$

where I_0 is the intensity at the interface and p is known as the evanescent wave penetration depth. The penetration depth, which characterizes the length scale of the
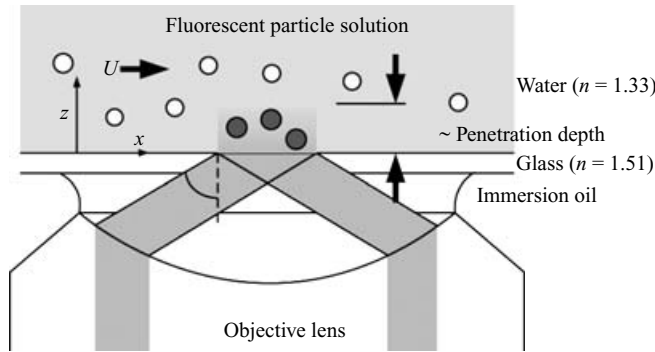
FIGURE 1. Objective-based total internal reflection fluorescence microscopy.

evanescent field, can be calculated from

$$p = \frac{\lambda_0}{4\pi} \left(n_1^2 \sin^2 \theta - n_2^2 \right)^{-1/2}, \tag{2.2}$$

where λ_0 is the wavelength of the incident light, θ is the beam incident angle and n_1 and n_2 are the indices of refraction of the solid and liquid, respectively.

2.2. *Emission intensity of fluorescent particles*

For spherical tracer particles with a uniform volumetric fluorophore distribution in an evanescent field, Kihm *et al.* (2004) calculated the particles emission intensities as an exponential function of their distances to a substrate surface. Through experience we have found, however, that the intensity of fluorescence emission from a large number of nominally identical particles can vary owing to a variety of factors, including statistical variations in illumination intensity, quantum efficiency of the imaging system and, most importantly, a distribution in the physical size of the particles. If we parameterize all of these variations by an 'effective emission radius', r, we can model the particle's probability density function (PDF) of its effective emission radius with a Gaussian distribution

$$P(r) = P_0 \exp \left[-\frac{(r/a - 1)^2}{\sigma_r^2} \right], \tag{2.3}$$

where a is the mean effective emission radius of the batch, σ_r is the characteristic variation (standard deviation) and P_0 is a normalization constant. Based on the calculation of Kihm *et al.* (2004) and the assumption that emission intensity of a fluorescent particle is proportional to the number of fluorophores within its volume, the emission intensity, I^e, of a particle in an evanescent field is

$$I^e(r, h) = \left(\frac{r}{a} \right)^3 \left[I_0^e e^{-(h-a)/d} \right], \tag{2.4}$$

where h is the distance from the particle's centre to the substrate surface at which total internal reflection occurs, I_0^e is the emitted intensity of a single particle with $r = a$ located at $h = a$ (i.e. touching the substrate surface), and d is an intensity decay length that need not be the same as the evanescent penetration depth. The intensity decay length can be obtained experimentally by statistically measuring intensities of particle as a function of particle distances from the substrate. Combining (2.3) and
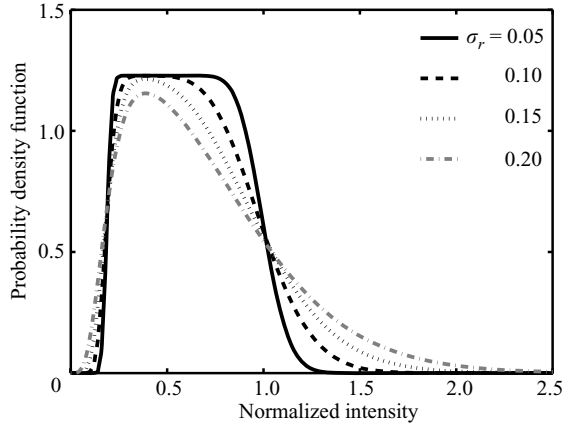
FIGURE 2. The emission intensity distribution of particles in a uniform concentration field. The normalized intensity in the horizontal axis is defined as I^e/I_0^e, and the calculation is performed with a normalized imaging range of $0 < h/a < 3$ and a normalized intensity decay length of $d/a = 1.8$.

(2.4), gives the joint PDF of the emitted intensity and a particle's distance to the substrate as

$$P(I^e, h) = \alpha \exp\left\{ -\frac{\left[\sqrt[3]{(I^e/I_0^e)\mathrm{e}^{(h-a)/d}} - 1\right]^2}{\sigma_r^2} \right\}. \tag{2.5}$$

When tracer particles are imaged, they would certainly be located at a range of distances from the substrate surface. The lower limit of this imaging range is $h = a$, representing a particle touching the substrate surface. The upper limit of the imaging range is determined by the sensitivity of the recording medium, such as an intensified CCD camera used in this study. For a given imaging range of $h_1 < h < h_2$, the PDF of a tracer particle's intensity is given by

$$P(I^e, h_1 < h < h_2) = \int_{h_1}^{h_2} P(I^e, h)c(h)\,\mathrm{d}h, \tag{2.6}$$

where $c(h)$ is the concentration profile of particles in the fluid. A sample plot of this distribution (2.6) is shown in figure 2 for a range of values of σ_r. For a low variation in effective emission radius (σ_r small), we see that the particles in the defined imaging range are sharply defined in intensity, with the brightest particles located at the surface ($I^e/I_0^e = 1$) and the faintest particles at the outer edge of the evanescent field ($I^e/I_0^e = 0.2$). However, as the variation in particle radius increases, the transitions become more blurred, and some larger particles close to the wall contribute to the long tail at high observed intensities, whereas small particles close to the edge of the imaging range are represented by the smooth transition close to $I^e/I_0^e = 0$.

When performing image analysis, however, one need not analyse all imaged particles. Instead, using particle intensity as a guide, one can choose to identify and analyse only the particles within a certain desirable intensity range, ignoring particles that appear too bright or too dim. Equation (2.5) could also describe the
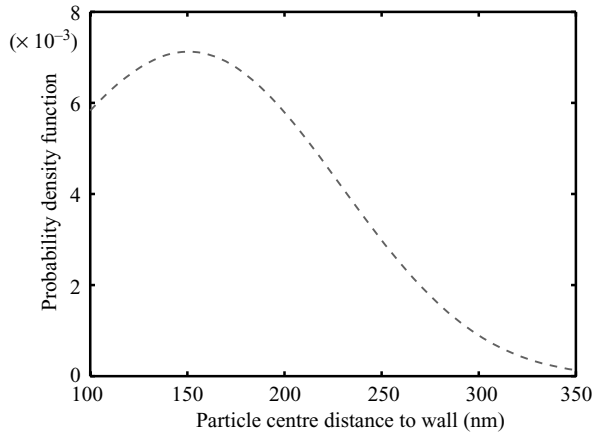
FIGURE 3. The predicted position distribution of particles with $0.5 < I^e/I_0^e < 1$ in a uniform concentration field. In this prediction, $a = 100$ nm, $d = 181$ nm and $\sigma_r = 0.18$.

particle position distribution within a normalized intensity range of $\alpha < I^e/I_0^e < \beta$ by

$$P(h, \alpha < I^e/I_0^e < \beta) = c(h) \int_\alpha^\beta P(I^e, h) \, \mathrm{d}\left(\frac{I^e}{I_0^e}\right). \tag{2.7}$$

An example of this position distribution (2.7) is shown in figure 3 for a normalized intensity range of $0.5 < I^e/I_0^e < 1$. The most obvious feature of figure 3 is that the distribution is non-uniform with the majority of particles contributing to this range of intensities coming from close to the substrate surface (<250 nm). In addition, the distribution has a long positive tail that gradually decays to zero far away into the fluid bulk. Because of the large-particle effective radius variation in this example, a large particle far away (for example, >300 nm) can exhibit the same fluorescence intensity as that of smaller particles close to the substrate surface. These observations reinforce the fact that a particle's intensity cannot be monotonically related to its distance to the solid surface, and attention should be given to any intensity-based quantitative analysis by recognizing the non-uniform position distribution and the contribution of particles far away from wall.

2.3. Near-surface shear flow

Although we are interested in determining the velocity of a pure fluid near a solid surface, we actually measure the velocity of small spheres near the surface, and it is important to recognize the differences between these two quantities. It is well known that shear and near-surface hydrodynamic effects can cause a tracer particle to rotate and translate at a velocity lower than the local velocity of the fluid in the same shear plane (Goldman, Cox & Brenner 1967b; Chaoui & Feuillebois 2003). Goldman *et al.* (1967b) proposed that a particle's translational velocity, U, in a shear flow with local shear rate, S, is given by

$$\frac{U}{hS} \simeq 1 - \frac{5}{16}\left(\frac{h}{r}\right)^{-3}, \tag{2.8}$$

valid for large h/r, and

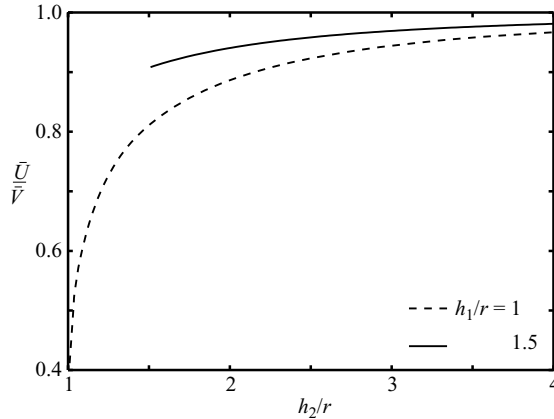$$\frac{U}{hS} \simeq \frac{0.7431}{0.6376 - 0.2\ln(h/r - 1)}, \tag{2.9}$$

FIGURE 4. The ratio of statistical apparent velocity of particles and mean fluid velocity under no-slip in an imaging range of $h_1 < h < h_2$, which is non-dimensionalized by particle radius. $\bar{V}$ is computed with linear fluid velocity profile, which is a good approximation near a surface. In the computation of $\bar{U}$, $c(h)$ is assumed to be uniform.

valid for small h/r. Although there exists no analytical approximation for intermediate values of h/r, Pierres *et al.* (2001) proposed a cubic approximation to numerical values presented by Goldman *et al.* (1967*b*):

$$\frac{U}{hS} \simeq \left(\frac{r}{h}\right) \exp\left\{0.68902 + 0.54756\left[\ln\left(\frac{h}{r} - 1\right)\right] + 0.072332\left[\ln\left(\frac{h}{r} - 1\right)\right]^2 \right.$$
$$\left. + 0.0037644\left[\ln\left(\frac{h}{r} - 1\right)\right]^3\right\}. \quad (2.10)$$

The apparent velocity, $\bar{U}$, of a large ensemble of particles chosen from a normalized intensity range of $\alpha < I^e/I_0^e < \beta$ and located in an imaging range of $h_1 < h < h_2$ is given by the average of the local velocity integrated over the imaging range:

$$\bar{U} = \frac{1}{h_2 - h_1} \int_{h_1}^{h_2} U(h, a, S(h)) P(h, \alpha < I^e/I_0^e < \beta) \, dh. \quad (2.11)$$

This average apparent velocity, $\bar{U}$, can be compared to the mean velocity of the pure fluid, $\bar{V}$, calculated for the same imaging range. The ratio of the two is shown in figure 4, from which we see that the average apparent velocity of particles is, not surprisingly, significantly lower than that of pure fluid velocity when the imaging range is very close to the substrate surface. This difference must be incorporated into the data analysis, and failure to recognize this effect can lead to misinterpretation of the measured data and underestimation of slip lengths.

It should be noted that (2.11) is based on a no-slip condition at the fluid/solid interface. If there exists a slip velocity, U_{slip}, at the solid boundary, the apparent velocity of the same ensemble of particles would be

$$\bar{U}_{app} = U_{slip} + \bar{U} = \delta S_w + \bar{U}, \quad (2.12)$$

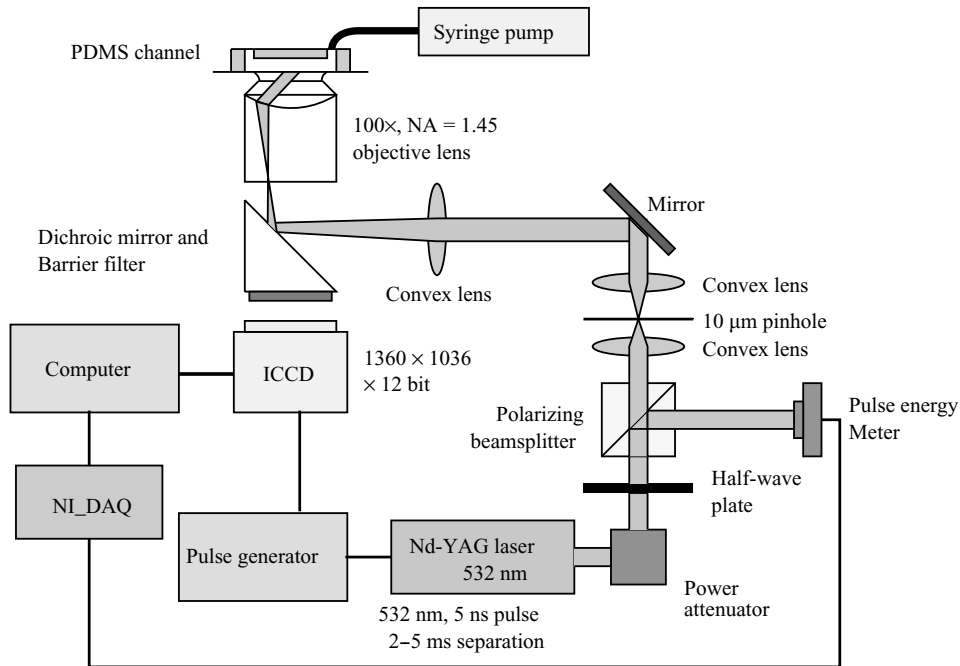where the slip velocity is characterized as the product of the slip length, δ, and the wall shear rate, S_w.

FIGURE 5. Image acquisition system.

3. Experimental procedure

3.1. *Materials and set-up*

Figure 5 shows the image acquisition system. Fluorescent particles were illuminated with an objective-based TIRFM method, as detailed in Jin *et al.* (2004). A pair of 532 nm, 5 ns laser pulses (Quantel Twins Q-Switched Double Pulse Nd:YAG Laser) were directed through a Nikon PL Apo NA 1.45 100X TIRF oil immersion objective at an angle that created total internal reflection at a glass–water interface, thus illuminating the near-surface region of water with an evanescent field (figure 1). Fluorescent images of near-surface particles were projected onto a Q-Imaging Intensified Retiga CCD camera (ICCD), capable of recording 1360×1036 pixels 12-bit images. Under $100\times$ magnification, each image pixel corresponds to 64.3 nm in the flow channel and the diffraction-limited spot size is 19.7 μm (calculated based on Meinhart & Wereley 2003). A TTL pulse generator (Berkeley Nucleonics Model 555) was used to synchronize laser pulses and image acquisitions. The energy of each illuminating laser pulse was recorded simultaneously with each image acquisition and this was used to adjust the resultant images and thus account for pulse-to-pulse variations in illumination intensity.

Test channels were fabricated using a polydimethylsiloxane (PDMS) (Dow Corning Sylgard 184) moulding technique (Duffy *et al.* 1998) and bonded onto polished glass wafers. The dimensions of the test channels were 50 ± 1 μm deep, 250 ± 1 μm wide and 15 mm long. To create hydrophilic microchannels, the pre-bonding PDMS surface was exposed to an oxygen plasma and immediately immersed in deionized water after bonding to a glass wafer. Hydrophobic channels, on the other hand, were fabricated by bonding untreated PDMS channels onto octadecyltrichlorosilane(OTS)-coated glass wafers. Detailed coating procedures can be found in Jin *et al.* (2004). It has been reported that water has a contact angle of 120° with a similarly prepared OTS-coating

(Tretheway & Meinhart 2002; Choi, Westin & Breuer 2002). The roughness of the test surface was measured using an atomic force microscope prior to bonding. The hydrophilic and hydrophobic surfaces had an r.m.s. surface roughness of 0.47 nm and 0.35 nm, respectively.

Monodisperse fluorescent polystyrene microspheres (Duke Scientific) with diameters of 200 nm (± 5 %) suspended in purified water (Fluka) at 0.04 % volume fraction were used as tracer particles in this experiment. These microspheres have a peak absorption wavelength of 542 nm and emit a red light at 612 nm. There were three reasons for selecting 200 nm diameter particles as probes in this experiment. First, smaller size fluorescent particles have a much larger size variation, making the relation of the particle centre distances from the solid wall and their fluorescent intensities less reliable. Secondly, smaller particles do not contain enough fluorophores to provide significant signals with a 5 ns laser illumination. Lastly, 200 nm particles do not diffuse too far during the interframe time, with diffusion out of the imaging range being our major concern.

A Harvard Apparatus 22 syringe pump was used to maintain particle solution flow rates, ranging from 1 to 10 μl min^{-1} (± 0.35 %). To maintain steady pumping motions of the Harvard Apparatus stepper motor, we introduced a large volume of air between the piston and the fluid in the syringe. This volume of air acted as a pressure shock absorber to damp out the oscillatory forcing of the syringe pump screw. In addition, a long tube (>1 m) was used to connect the syringe and the channel inlet. Particle flow motion was observed to be very steady under this set-up.

Twelve hundred images were captured at each flow rate, as well as in quiescent fluid. Once all necessary images of particle motion were captured, the test channel was filled with rhodamine-B solution. Images of the rhodamine-B solution were subsequently captured under the same evanescent illumination, and averaged to obtain an image characterizing the spatial distribution of the illuminating laser beam.

It has been suggested that nanobubbles and a gas bubble layer on hydrophobic surfaces could be alternative sources of apparent slip (Granick, Zhu & Lee 2003; Lauga & Brenner 2004; Lauga *et al.* 2005). Prior to each experiment, the fluid was degassed by placing the solution in a vacuum for at least 30 min. This procedure has been reported to eliminate nanobubble formation significantly (Zhang *et al.* 2004).

It is intuitive to assume that one can infer the location of a particle in the evanescent illumination field based on the fluorescence intensity. Kihm *et al.* (2004) used a ratiometric fluorescence intensity to track particle motions three-dimensionally. Although this is theoretically feasible, in practice, successful use of this technique requires precise knowledge of the illumination beam incident angle and a solution of Maxwell's equation for an evanescent field in a three-media system (glass, water and polystyrene), which can be difficult to express explicitly. Thus, an experimental method was devised to obtain a ratiometric relation between particle emission intensity and its distance to the glass surface. We attached individual fluorescent particles to fine tips of glass micropipettes, which were translated perpendicularly to the glass substrate in the evanescent field with a 0.4 nm precision stage (MadCity Nano-OP25). At each distance to the surface, 30 images of the attached particles were captured. The pixel values of the imaged particles were then averaged, and subsequently fitted to a two-dimensional Gaussian function to find their centre intensities. The process was repeated several times with different particles. The particle intensities are shown in figure 6, along with a exponential fit to the measured data:

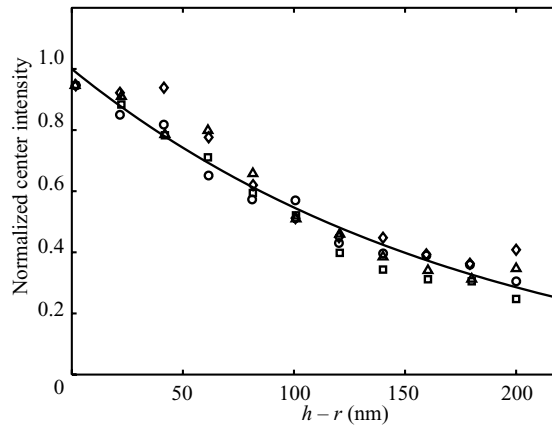$$I_{peak} = A e^{-\lambda(h-r)} + B, \qquad (3.1)$$

FIGURE 6. Fluorescent particle intensity as a function of its distance to the glass surface. The particles used here are 200 nm in diameter. The solid line is a least-squares exponential fit to the data whose decay length, λ, is 181 nm.

where A, B and λ are constants determined by a least-squares fit. The fitted curve predicts an intensity decay depth of 181 nm, very close to the evanescent penetration depth that we would predict based on the imaging lens, wavelength and refractive indices of the system.

3.2. *Velocimetry analysis*

The analysis of particle image pairs was performed using a custom particle-tracking program written in a MATLAB environment. Prior to velocimetry analysis, images of particles stuck on the glass substrate had to be removed from each image pair to prevent undesirable detection by the particle tracking velocimetry (PTV) algorithm. Although the presence of these stuck particles could distort the velocity field, they generally had a very low density and were usually placed at the edge of an image and far away from where the velocimetry measurements were performed. For each image, the signals due to stuck particles and background noise were removed by subtracting a reference image formed from the rolling average of 10 previous and 10 subsequent image pairs. To account for laser pulse energy fluctuation, every image was scaled by the measured laser illumination energy.

Velocimetry analysis started with finding the positions and peak intensities of all particles via threshold-identification and Gaussian fitting of the intensities of the pixels surrounding the peak. Subsequently, each particle's displacement was obtained with a limited-range nearest-neighbour matching, and the displacement was decomposed into streamwise and cross-stream components (for details of the tracking algorithm, see Jin *et al.* 2004). The particle seeding density was low enough for this tracking to be unambiguous. Intensities of the 'trackable' particles were converted to a normalized intensity ratio obtained by dividing the raw intensity counts by the average of all the stuck particles' initial intensity counts. Finally, particles within a desired normalized intensity range were selected for each flow rate and their mean streamwise velocity was defined as the apparent velocity of the ensemble. For the hindered diffusion analysis, the same analysis steps were followed except that diffusion coefficients of particles in quiescent fluid were obtained from the variance of displacements instead of velocities.
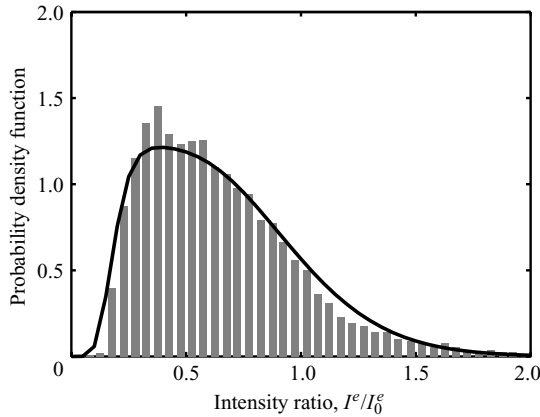
FIGURE 7. Observed fluorescent particle intensity distribution and its probability density function (PDF). The solid line represents the theoretical prediction (2.6) for an imaging range of 100 to 400 nm and a 15 % intensity statistical variation with a uniform concentration distribution of particles.

4. Results and discussion

4.1. *Validation of intensity calibration curve*

Figure 7 shows the distribution of particle intensities recorded during a typical data acquisition (in this case, in quiescent fluid). The accompanying solid line is the theoretical prediction (2.6), assuming an imaging range of 100–400 nm, and an effective emission radius variation of $\sigma_r = 0.15$. The good agreement between the observed and predicted intensity variation confirms our calibration results and the statistical theory of the observed particle intensities discussed earlier.

4.2. *Hindered diffusion*

Near-surface tracer particles are known to exhibit anisotropic hindered diffusion owing to hydrodynamic effects, and the hindered diffusion coefficient in the direction parallel to the substrate surface $D_\parallel$ is (Goldman, Cox & Brenner 1967*a*)

$$\frac{D_\parallel}{D_0} = 1 - \frac{9}{16}\left(\frac{h}{r}\right)^{-1} + \frac{1}{8}\left(\frac{h}{r}\right)^{-3} - \frac{45}{256}\left(\frac{h}{r}\right)^{-4} - \frac{1}{16}\left(\frac{h}{r}\right)^{-5} + O\left(\frac{h}{r}\right)^{-6}, \quad (4.1)$$

where D_0 is the Stokes–Einstein diffusivity of a spherical particle in the fluid bulk. This 'method of reflection' approximation is generally valid for $(h - r)/r > 1$. For $(h - r)/r < 1$, Goldman *et al.* (1967*b*) proposed an asymptotic solution,

$$\frac{D_\parallel}{D_0} = -\frac{2[\ln((h-r)/r) - 0.9543]}{[\ln((h-r)/r)]^2 - 4.325\ln((h-r)/r) + 1.591}. \quad (4.2)$$

The combination of our particle-tracking algorithm and the intensity calibration curve was applied to analyse near-surface particle Brownian motion parallel to the glass substrate. The results are compared to the methods of reflection calculation (4.1) and shown in figure 8. The experimental data show reasonably good agreement with the theory, including the fall in the effective diffusion coefficient close to the surface. The results further improve our confidence in the overall experimental method and subsequent analysis.
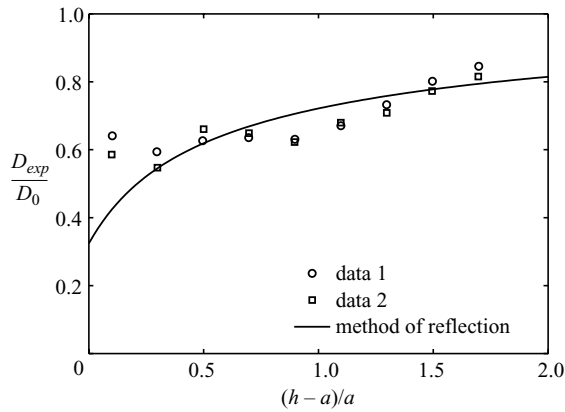
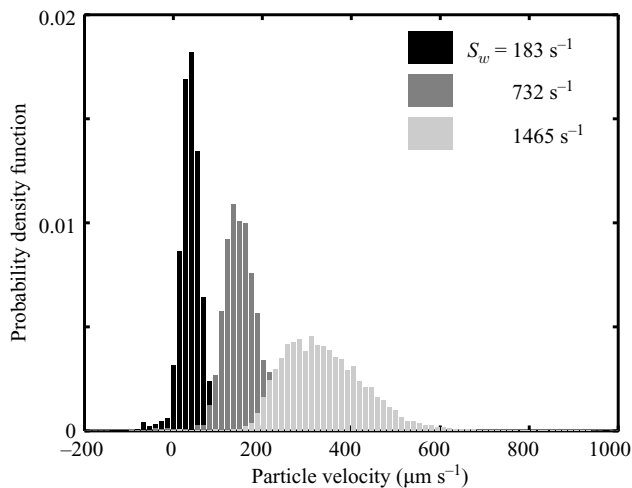FIGURE 8. Ratio of hindered diffusion coefficients (D_{exp}) for Brownian motion parallel to a surface.

FIGURE 9. Distribution of observed particle streamwise velocities under various shear rates. Data include measurements of flow over a hydrophobic surface.

4.3. *Velocity distributions of particles*

Figure 9 shows distributions of particle velocities at three different shear rates. Note that the streamwise velocity distributions widen as the shear rate increases, and their asymmetric shapes show an increasing skewness as the shear rate increases. The increasing distribution width and skewness at high shear rates are both results of sampling particle displacements from an imaging range with finite thickness (Jin *et al.* 2004). Physically, at higher shear rates, the finite-thickness imaging range contains particles that are translated by a wider range of local velocities, hence the increasing width of the apparent velocity distributions. In addition, because the particles are confined by the solid wall, they are more likely to move away from the wall and into a faster-moving shear plane. Thus, the distribution exhibits a more pronounced positive skewness at the higher shear rates.
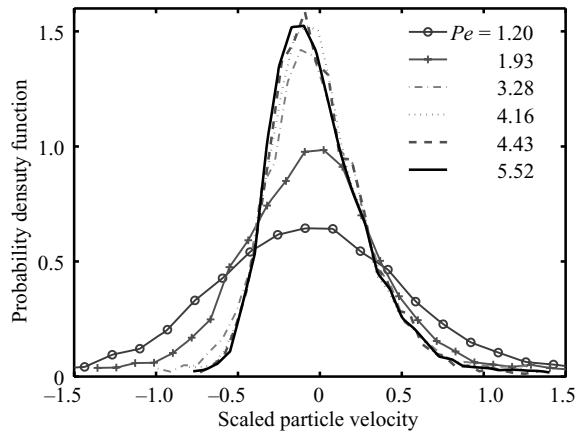
FIGURE 10. Distribution of observed particle streamwise velocities after scaling the velocity distributions in figure 9. The velocities are scaled according to (4.4). *Pe* of 1.20, 3.28 and 4.43 correspond to the shear rates of 183, 732 and 1465 s^{-1} in figure 9, respectively.

The effect of shear with a finite-thickness imaging range can be characterized if the streamwise particle velocity in figure 9, V, is scaled by

$$\tilde{V} = \frac{V - \langle V \rangle}{\langle V \rangle}, \tag{4.3}$$

where $\tilde{V}$ is the scaled streamwise particle velocity and $\langle V \rangle$ is the mean value of each velocity distribution. The scaled velocity distributions are shown in figure 10. At each shear rate, the relative contributions of velocities from shear flow and Brownian motion can be characterized by the Péclet number, *Pe*. Here, the Péclet number is defined as the ratio of the shear-induced displacement, L, to the diffusive displacement, s, during the interframe time period, Δt,

$$Pe = \frac{L}{s} = \frac{\langle V \rangle \Delta t}{\sqrt{2D_0 \Delta t}}. \tag{4.4}$$

Because $\langle V \rangle$ is shear-dependent only, the shear-induced effects in all velocity distributions in figure 10 are scaled to equal magnitudes. It can be seen that small Péclet numbers are associated with greater distribution widths, whereas the distributions collapse onto a single skewed distribution at high Péclet numbers. The explanation is that at low Péclet numbers, the distribution widths scale inversely to shear, suggesting a diffusion dominance and thus the large widths of the velocity distributions are due to Brownian motion. As the Péclet number increases, the effect of shear flow on particle motion increases and when $Pe > 3$, particle motions are completely shear-dominant, causing the distributions to overlap. It should be noted that the overlapping distributions have the same distribution width, asymmetric shape and the same positive tail, which are absent in small-Péclet-number cases. These observations confirm the explanation that in figure 9, the increasing distribution width and skewness at high shear rates are both effects of shear.

4.4. *Measurements of apparent slip velocities*

For each flow case, the intensity distribution of all 'trackable' particles were compared to the theoretical prediction (2.6) to identify the unknown parameters such as h_1, h_2 and σ_r through optimization, as demonstrated in §4.1 and figure 7. With these
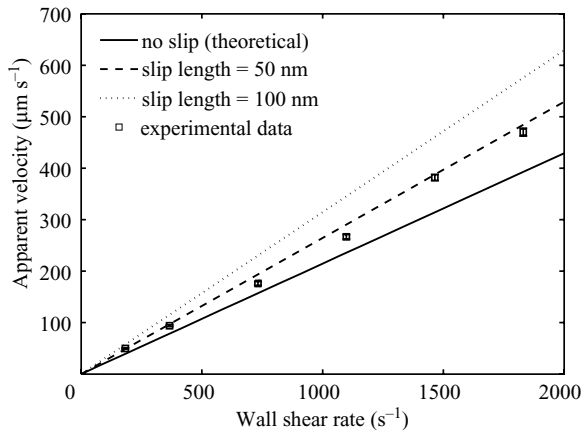
FIGURE 11. Experimental apparent velocity of particles in a shear flow over a hydrophilic surface ($0.21 < I^e/I_0^e < 0.78$), and its comparison to slopes of expected apparent velocities if there exists a 0, 50 or 100 nm slip length. The error bar of each experimental data point represents a 95 % confidence interval. In all cases, the 95 % confidence intervals are within ± 3 % of the reported mean velocity values.

FIGURE 12. Experimental apparent velocity of particles in a shear flow over a hydrophobic surface ($0.5 < I^e/I_0^e < 1.0$), and its comparison to slopes of expected apparent velocities if there exists a 0, 50 or 100 nm slip length. The error bar of each experimental data point represents a 95 % confidence interval. In all cases, the 95 % confidence intervals are within ± 3 % of the reported mean velocity values. Key as in figure 11.
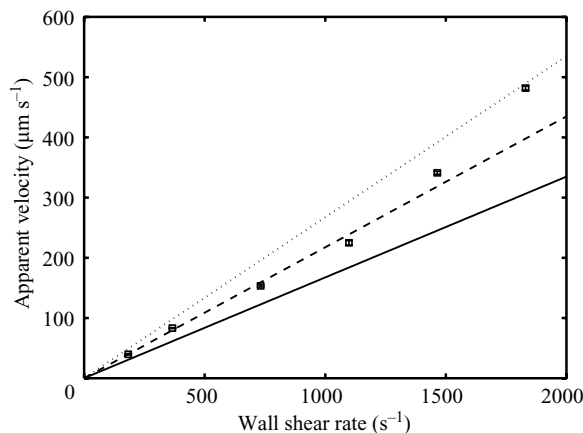
parameters known, we calculated the theoretical apparent velocities of a particle ensemble, chosen from a normalized intensity range, by using equation (2.12) and varying the slip length conditions. Subsequently, these velocities were compared to the experimental apparent velocities (mean values of the streamwise velocity distribution) of particles from the same normalized intensity range to extract experimental slip velocities and slip lengths.

Figures 11 and 12 show the experimental and theoretical apparent velocities as a function of wall shear rate over hydrophilic and hydrophobic surfaces, respectively. In both figures, the solid lines represent the theoretical apparent velocities assuming zero slip (equation (2.11)). The dashed and dotted lines are the expected apparent velocities
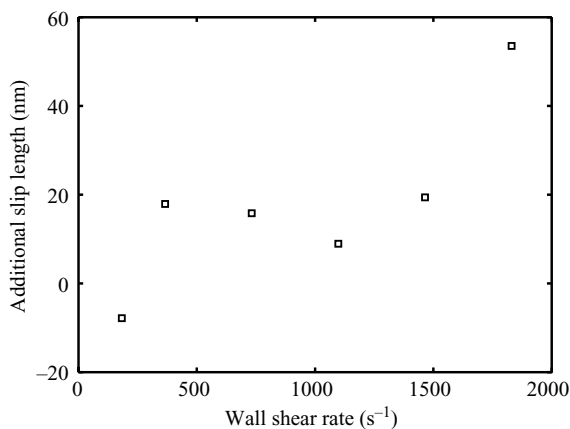
FIGURE 13. The additional slip length due to surface hydrophobicity.

if we were to assume a 50 nm and a 100 nm slip length, respectively (calculated using (2.12)). In the case of the hydrophilic surface (figure 11), the measured slip length ranges from 26 to 57 nm with a slightly increasing trend as the wall shear rate increases. The data obtained for flow over the hydrophobic surface (figure 12), on the other hand, suggest a larger slip length ranging from 37 to 96 nm, with a more observable increasing trend of wall-shear-rate dependence at higher shear rates. A quantitative comparison of the two cases shows a slip length attributed to surface hydrophobicity ranging from −7 nm at low shear rates to 54 nm at the highest tested shear rate, with an average value of 16 nm (figure 13). The additional slip caused by surface hydrophobicity is in agreement with many experimental results (Zhu & Granick 2002; Choi *et al.* 2003; Cottin-Bizonne *et al.* 2005*b*; Joseph & Tabeling 2005), but is in sharp disagreement with others (Zhu & Granick 2001; Tretheway & Meinhart 2002; Lumma *et al.* 2003).

There are three possible sources of measurement uncertainty in figures 11 and 12: determination of (*a*) the wall shear rate, (*b*) the apparent velocities of particle ensembles and (*c*) the imaging range. Because wall shear rates are calculated based on microchannel dimensions and flow rates which are controlled by the syringe pump, we estimate that the uncertainty in the wall shear rates is less than 3 %. If there is significant slip at the wall, the shear rates could be slightly lower than the reported values. However, the largest observed slip length is less than 1 % of the channel height, and thus the slip effect on wall shear rate calculation can be safely neglected. The determination of apparent velocities of particle ensembles also has extremely low uncertainty because the central limit theorem constrains the statistical mean of a large sample (a few thousand trackings) to a very low uncertainty ($< \pm 3$ % of the reported velocity values for 95 % confidence intervals). In addition, with subpixel resolution of the particle centre detection, our PTV algorithm is able to track particle displacements with high accuracy (< 0.1 pixel, Cheezum, Walker & Guilford 2001). The largest source of uncertainty is the determination of the imaging range. The imaging range is determined statistically based on the particle intensity decay length obtained from figure 6 where intensity measurements were performed in increments of 20 nm, which could serve as the upper limit of imaging range uncertainty. However, it should be noted that, with an uncertainty of 20 nm taken into consideration, the largest measured slip length still will not exceed 150 nm – much smaller than other experimental studies which reported slip lengths greater than a few hundred nanometres.

Note that the corrections due to shear-induced rotation (figures 11 and 12) do not account for the possibility of slip between the fluid and the tracer particle, and we are unaware of any work that extends the theory of Goldman *et al.* (1967*b*) to include the effect of surface slip. Physically, surface slip is unlikely to be an issue, because the tracer particles have relatively rough surfaces. Nevertheless, we can qualitatively estimate its effect. Slip between the fluid and the tracer particle will modify the particle velocity in two ways. First, the reduced shear force will result in the particle velocity lagging the local fluid velocity. Secondly, however, slip will reduce the shear-induced rotation of the particle. Since these two mechanisms act in opposition to each other, we believe that, as a first approximation, we can ignore this effect.

Granick *et al.* (2003) and Lauga *et al.* (2005) both pointed out that large surface roughness can significantly decrease slip. The slip length we measured with sub-nanometer surface roughness, however, agrees well with the surface-roughness dependency reported by Zhu & Granick (2002). It should also be noted that Joseph & Tabeling (2005), with flow experiments conducted under similar surface roughness, hydrophobic coating and shear rates, reported slip length very close to the present results. It has also been suggested that electrokinetic effects could significantly affect velocimetry measurements of suspended particles close to a surface. Lauga (2004) reports that a streaming potential can induce electrophoretic motion of particles if particle surfaces are charged, and applying this theory to the current conditions results in an 'apparent' slip length of at most 18 nm.

Electrostatic interaction between tracer particles and surface could also affect accuracy of velocimetry measurements (Lauga *et al.* 2005). If the tracer particles and the substrate surface are similarly charged, electrostatic repulsion can create a depletion layer near the substrate surface that effectively shifts the imaging range. Because the slip length calculations in figures 11 and 12 are based on the assumption that particle concentration is uniform near the surface, a depletion layer could be a source of 'apparent slip' if it is not recognized. Lumma *et al.* (2003) suggested that the depletion-layer thickness can be as large as 0.9 μm for a pure water and glass combination. Such a thickness seems unreasonably large as it is much bigger than the evanescent field penetration depth and consequently few fluorescent particles would be observed. In contrast, Flicker, Tipa & Bike (1993) experimentally measured the depletion-layer thickness to be of the order of 10 to 30 nm. For our experimental set-up, calculations suggest that, based on the overall particle seeding density, if the particles are uniformly distributed in the fluid, we should be able to see around 19 particles in a 26 μm × 26 μm image field. This is in close agreement with our experimentally derived images, and we can conclude that the depletion-layer thickness must be much smaller than our imaging range and thus effects due to a depletion-layer thickness of this magnitude would not be detectable with our current imaging technique. However, recognizing the possibility of such a depletion layer's existence, we re-analysed the theoretical curves in figures 11 and 12 by assuming an imaging range farther away from the substrate surface. We found such a shift would result in higher theoretical apparent velocities of particle ensembles and therefore lower slip lengths for all shear rates, suggesting that our reported slip lengths are most probably the upper bound of the true slip length value.

The electrostatic and electrokinetic interactions are an interesting pair as their significance decreases with increasing ionic strength of the test fluid. Perhaps a more accurate direct measurement of the true surface slip could be obtained if aqueous solutions of moderately high ionic strengths were used.

5. Conclusions

The results presented here represent direct measurements of local velocities in the near-wall region of a fluid–solid boundary. Despite the relative simplicity of the experiment, several subtle issues must be addressed, including the spatial non-uniformity of the illumination region, the effects of the local shear on the dynamics of seeding particles, and the statistical variations in the effective visibility of the seeding particles. The current experiment confirms previous measurements in our own group (Choi *et al.* 2003) as well as some other recent measurements (Zhu & Granick 2002; Joseph & Tabeling 2005) that there is minimal slip over hydrophilic surfaces, and that hydrophobic surfaces do appear to introduce a discernible, but small boundary slip.

Although the present technique allows for measurement of particle motions very close to the solid surface, it suffers from some limitations and there is room for improvement. Most notably, the tracking in the wall-normal direction is currently limited to an accuracy of approximately 10 % of the evanescent penetration depth (about 20 nm in the current case). If particles with a higher degree of monodispersity can be reliably found, and if the imaging system noise can be reduced (both of which are technical improvements on the immediate horizon), we believe that the technique can be used to track particles with an order of magnitude improvement in accuracy. However, even with the current levels of uncertainty, there is no possibility that the flow exhibits a slip length more than 150 nm (figure 12) over the range of shear rates tested.

While the debate of slip versus no-slip will probably continue in the foreseeable future, we believe that a consensus is forming from more recent experiments that the slip effect is not as extreme as some studies might have suggested. As many authors have pointed out, measurement and interpretation of slip data in the nanoscale can be difficult because other physical phenomena, such as electrokinetics and nanobubbles, might lead to observations of an 'apparent slip' caused by other complicating factors. All of these suggest that close attention must be to paid to documenting the experimental conditions, and that this might well reveal the reasons behind the range of reported apparent slip phenomena.

REFERENCES

Axelrod, D. 2001 Total internal reflection fluorescence microscopy in cell biology. *Traffic* **2**, 764–774.

Barrat, J.-L. & Bocquet, L. 1999 Large slip effect at a nonwetting fluid–solid interface. *Phys. Rev. Lett.* **82**, 4671–4674.

Burmeister, J. S., Olivier, L. A., Reichert, W. M. & Truskey, G. A. 1998 Application of total internal reflection fluorescence microscopy to study cell adhesion to biomaterials. *Biomaterials* **19**, 307–325.

Chaoui, M. & Feuillebois, F. 2003 Creeping flow around a sphere in a shear flow close to a wall. *Q. J. Mech. Appl. Maths* **56**, 381–410.

Cheezum, M. K., Walker, W. F. & Guilford, W. H. 2001 Quantitative comparison of algorithms for tracking single fluorescent particles. *Biophys. J.* **81**, 2378–2388.

CHOI, C.-H., WESTIN, K. J. A. & BREUER, K. S. 2002 To slip or not to slip – water flows in hydrophilic and hydrophobic microchannels. In *Proc. IMECE 2002*, pp. IMECE2002–33707.

CHOI, C.-H., WESTIN, J. A. & BREUER, K. S. 2003 Apparent slip flows in hydrophilic and hydrophobic microchannels. *Phys. Fluids* **15**, 2897–2902.

CIEPLAK, M., KOPLIK, J. & BANAVAR, J. R. 2001 Boundary conditions at a fluid–solid surface. *Phys. Rev. Lett.* **86**, 803–806.

COTTIN-BIZONNE, C., BARRAT, J.-L., BOCQUET, L. & CHARLAIZ, E. 2005a Low-friction flows of liquid at nanopatterned interfaces. *Nature Materials* **2**, 237–240.

COTTIN-BIZONNE, C., CROSS, B., STEINBERGER, A. & CHARLAIZ, E. 2005b Boundary slip on smooth hydrophobic surfaces: intrinsic effects and possible artifacts. *Phys. Rev. Lett.* **94**, 056102.

DUFFY, D. C., McDONALD, J. C., SCHUELLER, O. J. A. & WHITESIDES, G. M. 1998 Rapid prototyping of microfluidic systems in poly(dimethylsiloxane). *Anal. Chem.* **70**, 4974–4984.

FLICKER, S. G., TIPA, J. L. & BIKE, S. G. 1993 Quantifying double-layer repulsion between a colloidal sphere and a glass plate using total internal reflection microscopy. *J. Colloid Interface Sci.* **158**, 317–325.

GALEA, T. M. & ATTARD, P. 2004 Molecular dynamics study of the effect of atomic roughness on the slip length at the fluid–solid boundary during shear flow. *Langmuir* **20**, 3477–3482.

GOLDMAN, A. J., COX, R. G. & BRENNER, H. 1967a Slow viscous motion of a sphere parallel to a plane wall–i: motion through a quiescent fluid. *Chem. Engng Sci.* **22**, 637–651.

GOLDMAN, A. J., COX, R. G. & BRENNER, H. 1967b Slow viscous motion of a sphere parallel to a plane wall – ii: Couette flow. *Chem. Engng Sci.* **22**, 653–660.

GRANICK, S., ZHU, Y. & LEE, H. 2003 Slippery questions about complex fluids flowing past solids. *Nature Materials* **2**, 221–227.

HOSODA, M., SAKAI, K. & TAKAGI, K. 1998 Measurement of anisotropic Brownian motion near an interface by evanescent light-scattering spectroscopy. *Phys. Rev. E* **58**, 6275–6280.

JIN, S., HUANG, P., PARK, J., YOO, J. Y. & BREUER, K. S. 2004 Near-surface velocimetry using evanescent wave illumination. *Exps. Fluids* **37**, 825–833.

JOSEPH, P. & TABELING, P. 2005 Direct measurement of the apparent slip length. *Phys. Rev. E* **71**, 035303(R).

KIHM, K. D., BANERJEE, A., CHOI, C. K. & TAKAGI, T. 2004 Near-wall hindered Brownian diffusion of nanoparticles examined by three-dimensional ratiometric total internal reflection fluorescence microscopy (3-d r-tirfm). *Exps. Fluids* **37**, 811–824.

LAUGA, E. 2004 Apparent slip due to the motion of suspended particles in flows of electrolyte solutions. *Langmuir* **20**, 8924–8930.

LAUGA, E. & BRENNER, M. P. 2004 Dynamic mechanisms for apparent slip on hydrophobic surfaces. *Phys. Rev. E* **70**, 026311.

LAUGA, E., BRENNER, M. P. & STONE, H. A. 2005 Microfluidics: The no-slip boundary condition. In *Handbook of Experimental Fluid Dynamics* (ed. J. Foss, C. Tropea & A. Yarin), chap. 15. Springer.

LUMMA, D., BEST, A., GANSEN, A., FEUILLEBOIS, F., RADLER, J. O. & VINOGRADOVA, O. I. 2003 Flow profile near a wall measured by double-focus fluorescence cross-correlation. *Phys. Rev. E* **67**, 056313.

MEINHART, C. D. & WERELEY, S. T. 2003 The theory of diffraction-limited resolution in microparticles image velocimetry. *Meas. Sci. Technol.* **14**, 1047–1053.

NAGAYAMA, G. & CHENG, P. 2004 Effects of interface wettability on microscale flow by molecular dynamics simulation. *Intl J. Heat Mass Transfer* **47**, 501–513.

NETO, C., CRAIG, V. S. J. & WILLIAMS, D. R. M. 2003 Evidence of shear-dependent boundary slip in Newtonian liquids. *Eur. Phys. J. E* **12**, S71–S74.

PIERRES, A., BENOLIEL, A.-M., ZHU, C. & BONGRAND, P. 2001 Diffusion of microspheres in shear flow near a wall: use to measure binding rates between attached molecules. *Biophys. J.* **81**, 25–42.

PIT, R., HERVET, H. & LEGER, L. 2000 Direct experimental evidence of slip in hexadecane: solid interface. *Phys. Rev. Lett.* **85**, 980–983.

SADR, R., LI, H. & YODA, M. 2005 Impact of hindered Brownian diffusion on the accuracy of particle-image velocimetry using evanescent-wave illumination. *Exps. Fluids* **38**, 90–98.

SCHNELL, E. 1956 Slippage of water over nonwettable surfaces. *J. Appl. Phys.* **27**, 1149–1152.

THOMPSON, N. L. & LANGERHOLM, B. C. 1997 Total internal reflection fluorescence: applications in cellular biophysics. *Current Opinion Biotech.* **8**, 58–64.

THOMPSON, P. A. & TROIAN, S. M. 1997 A general boundary condition for liquid flow at solid surfaces. *Nature* **389**, 360–362.

TOOMRE, D. & MANSTEIN, D. J. 2001 Lighting up the cell surface with evanescent wave microscopy. *Trends Cell Biol.* **11**, 298–303.

TRETHEWAY, D. C. & MEINHART, C. D. 2002 Apparent fluid slip at hydrophobic microchannel walls. *Phys. Fluids* **14**, L9–L12.

WATANABE, K., YANUAR & MIZUNUMA, H. 1998 Slip of Newtonian fluids at solid boundary. *JSME Intl J.* **41**, 525–529.

ZETTNER, C. M. & YODA, M. 2003 Particle velocity field measurements in a near–wall flow using evanescent wave illumination. *Exps. Fluids* **34**, 115–121.

ZHANG, X. H., ZHANG, X. D., LOU, S. T., ZHANG, Z. X., SUN, J. L. & HU, J. 2004 Degassing and temperature effects on the formation of nanobubbles at the mica/water interface. *Langmuir* **20**, 3813–3815.

ZHU, Y. & GRANICK, S. 2001 Rate–dependent slip of Newtonian liquid at smooth surfaces. *Phys. Rev. Lett.* **87**, 096105.

ZHU, Y. & GRANICK, S. 2002 Limits of the hydrodynamic no-slip boundary condition. *Phys. Rev. Lett.* **88**, 106102.